# Size driven barrier to chirality reversal in electric control of magnetic vortices in ferromagnetic nanodiscs

W. A. S. Aldulaimi[1], M. B. Okatan[2], K. Sendur[1], M. C. Onbasli[3] and I. B. Misirlioglu[1, 4]

[1] Faculty of Engineering and Natural Sciences, Sabanci University, Orhanli/Tuzla 34956 Istanbul, Turkey

[2] Department of Materials Science and Engineering, Izmir Institute of Technology, Gulbahce/Urla, 35430 Izmir, Turkey

[3] Department of Electrical & Electronics Engineering, Koc University 34450 Istanbul, Turkey

[4] Center of Excellence for Functional Surfaces and Interfaces for Nano-Diagnostics (EFSUN), Sabanci University, Orhanli, 34956, Tuzla, Istanbul, Turkey

## 1. Energy terms in the LLG approach

$H_{eff}$ includes the external and the internal fields derived from the magnetic energy density, E:

$$H_{eff} = -\frac{\partial E}{\mu_0 \partial M} = H_{exch} + H_{demag} + H_{ani} + H_{Zeeman}$$

Uniform 6-neighbor exchange field. The exchange field contribution from cell $(i,j,k)$ is given by:

$$H_{exch}(i,j,k) = \frac{2A}{\mu_0 M_s} \sum_i^N \frac{m(i',j',K') - m(i,j,k)}{\Delta^2}$$

Where $N$ is the set consisting of 6 cells neighboring to cell $(i,j,k)$, A is the exchange coefficient between cells $(i,j,k)$ and $(i',j',K')$ in J/m, and $\Delta^2$ is the discretization step size between cells $(i,j,k)$ and $(i',j',K')$ in meters [1]. The exchange energy density of a single computational cell can be obtained from the equation:

$$E_{exch}(i,j,k) = A \sum_i^N \frac{m(i,j,k) \cdot (m(i,j,k) - m(i',j',k'))}{\Delta^2}$$

The demagnetization field for each computational cell is calculated as:

$$H_{demag}(i,j,k) = \frac{M_s}{4\pi} \sum_{i'=1}^{N_x} \sum_{j'=1}^{N_y} \sum_{k'=1}^{N_z} (C(i,j,k,i',j',k') \cdot m(i',j',k'))$$

Here, Nx, Ny, Nz are the grid dimensions in x, y, z direction, respectively, and $C(i,j,k,i',j',k')$ is a space-dependent matrix.

$$c(i,j,k,i',j',k') = \begin{bmatrix} K_{xx} & K_{xy} & K_{xz} \\ K_{yx} & K_{yy} & K_{yz} \\ K_{zx} & K_{zy} & K_{zz} \end{bmatrix}$$

The demagnetization energy density of a single computational cell can be obtained from the following equation:

$$E_{demag}(i,j,k) = -\frac{1}{2}\mu_0 M_s (H\_demag(i,j,k) \cdot m(i,j,k))$$

For each computational cell, the anisotropy field is given by [1]:

In the case of the uniaxial anisotropy:

$$H_{ani}(i,j,k) = \frac{2K_1}{\mu_0 M_s}(m(i,j,k) \cdot n)n$$

where $K_1$ is the material anisotropy coefficient, $n$ is the anisotropy axis. If $K_1 > 0$, $n$ is the easy axis, and if $K_1 < 0$, $n$ is normal to the easy plane.

In the case of the cubic anisotropy:

$$H_{ani}(i,j,k) = -\frac{2D(i,j,k)}{\mu_0 M_s} m(i,j,k)$$

Here, $D(i,j,k)$ is the space-dependent matrix, which is calculated as shown below:

$$D = \begin{bmatrix} K_1(m_y^2 + m_z^2) & 0 & 0 \\ 0 & K_1(m_x^2 + m_z^2) & 0 \\ 0 & 0 & K_1(m_x^2 + m_y^2) \end{bmatrix}$$

For both cases, the anisotropy energy density (in J/m³) of a single computational cell can be obtained from the following equation:

$$E_{ani}(i,j,k) = -\frac{1}{2}\mu_0 M_s (H_{ani}(i,j,k) \cdot m(i,j,k))$$

The energy density of a single computational cell associated with the Zeeman field can be obtained from:

$$E_{zeeman}(i,j,k) = -\mu_0 M_s (H_{zeeman}(i,j,k) \cdot m(i,j,k))$$

## 2. Computation of the chirality

We obtain the chirality from the following equation:

$$Chirality = \frac{1}{n}\oint m \cdot dl$$

where $m$ is normalized magnetization ($\frac{M}{M_s}$), $dl$ is the arc length of the path which was chosen as the circle around the center of the disc, and $n$ is the number of sites over which the integral is evaluated, for example, $n = 4$ in the following Fig. S1.
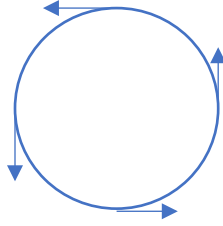


**Figure S1**. Circular bilinear interpolation path over a total of 4 point coordinates and the trajectories at these coordinates. The number of points at which trajectories can be considered over the circular path can be increased for better resolution.

In our calculation, n was chosen as 720, and M values on a given path were determined via bilinear interpolation, a method used to form continuous curves on a discrete set of data points, especially when one has to evaluate an analytical expression such as in the case of chirality defined as an integral over a closed continuous path. Multiple circles were constructed around the center of the disc and for each layer of the disc and the average value was taken as the Chirality value given in Fig. 4 in the manuscript.

3. **The electric flux direction and the induced magnetic field**
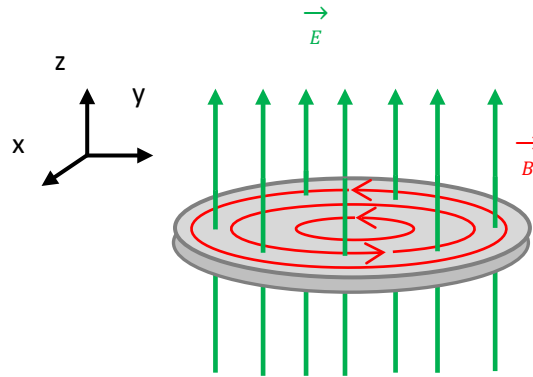


**Figure S2**. The applied time-varying electric flux is perpendicular to permalloy nanodisc along the z-axis (green vectors) and the induced magnetic field in-plane (XY-plane, red vectors) as a result of the electric field.

4. **Energy density comparison (10 nm, 20 nm, 30 nm and 40 nm thick discs)**

Looking at Fig. S3, no switching was induced in 10 nm thick disc for the prescribed pulse (Fig. 3(a)); therefore, no peak in energy, which signals chirality reversal, was observed. Thicker discs (20, 30 and 40 nm) undergo chirality reversal and the energy peak amplitudes decrease with increasing disc thickness, implying that the magnetic moments "realign" collectively in an easier manner during the reversal process, meaning less deviation from the parallel alignment and hence a smaller exchange energy peak. However, albeit the vortex state consists of dipoles mostly nested on the x-y axes (disc plane) the collective movement during reversal also generates a transient component along the z-axis, which causes an increase in the demagnetization field, hence the demagnetization energy signaled by the energy peak as shown in in Fig. S3. Notice the slight reduction in the demagnetization energy in the 20, 30 and 40 nm thick discs with increasing disc thickness.
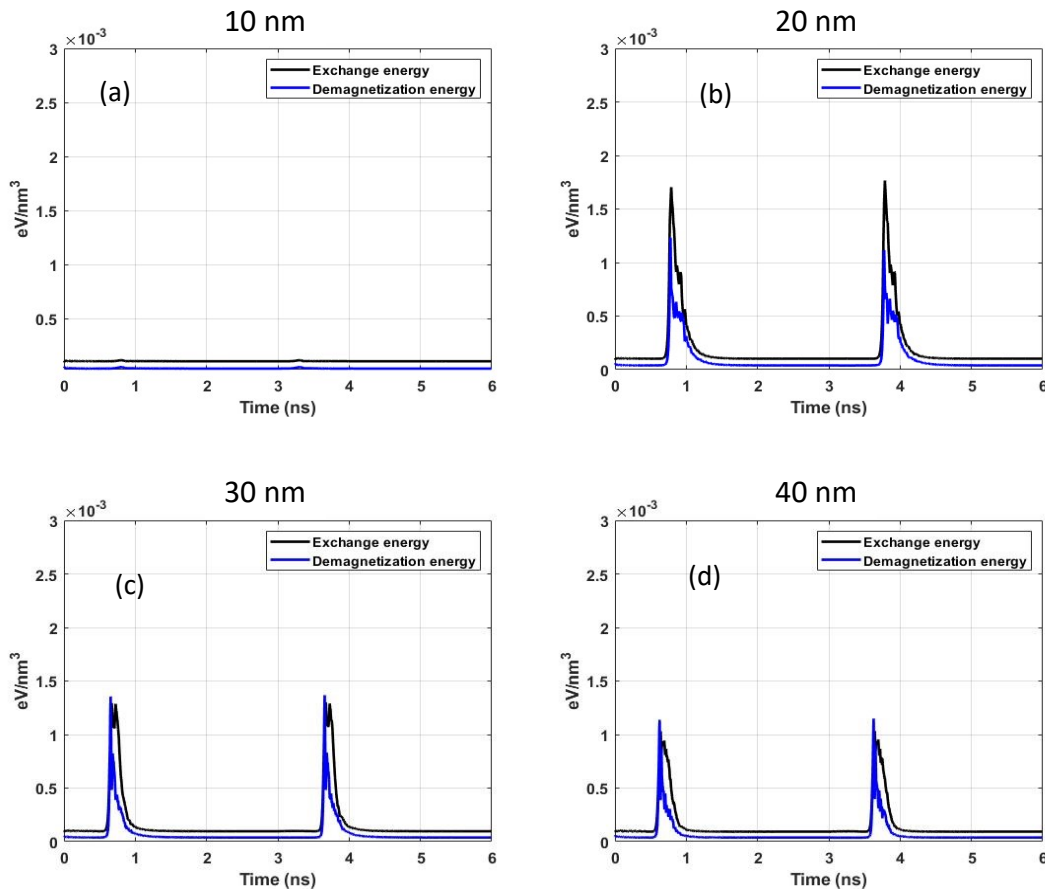


**Figure S3**. Comparison of the exchange and demagnetization energy terms in (a) 10 nm thick disc, (b) 20 nm thick disc thick, (c) 30 nm thick disc, and (d) 40 nm thick disc under the pulses provided in Figure 3(a) in the manuscript.

## 5. Formation of the vortex-antivortex (v-av) lattice

The appearance of the v-av lattice as a transient state during switching of the 10 nm disc is given in the following mp4 files that were generated using the data of our simulations:

a. The file entitled "**metastable state 1.mp4**" considers two consecutive pulses separated by a time interval.

b. The file entitled "**metastable state 2.mp4**" considers only one pulse followed by the subsequent relaxation of the system.

## 6. Polarity-chirality correlation

We provide chirality and polarity reversal results for 10 nm, 20 nm, 30 nm, and 40 nm thick discs wherein we applied an electric field pulse to induce chirality reversal of $E_{01} = 2 \, V/nm$ (See pulse shape in Fig. 3(a) in the original manuscript). We do so to also confirm that thickness impacts the chirality reversal process due to the barriers reduced with increasing disc thickness (See Fig. S3), as well as checking the relation between polarity and chirality. Defining a term such as sgn(p)×sgn(c) where we basically multiply the sign of polarity with the sign of chirality, neglecting their specific values, one can shed light on the polarity-chirality relation. By tracking this product, we can tell if there is a "coupled chirality-polarity" switching for 10 nm, 20 nm 30 nm, and 40 nm thick discs during the reversal process. If the sgn(p)×sgn(c) remains constant, this would mean that chirality and polarity are coupled, i. e., they switch together under an applied pulse. We have plotted the results for 10 nm, 20 nm, 30 nm, and 40 nm discs in Fig. S4.
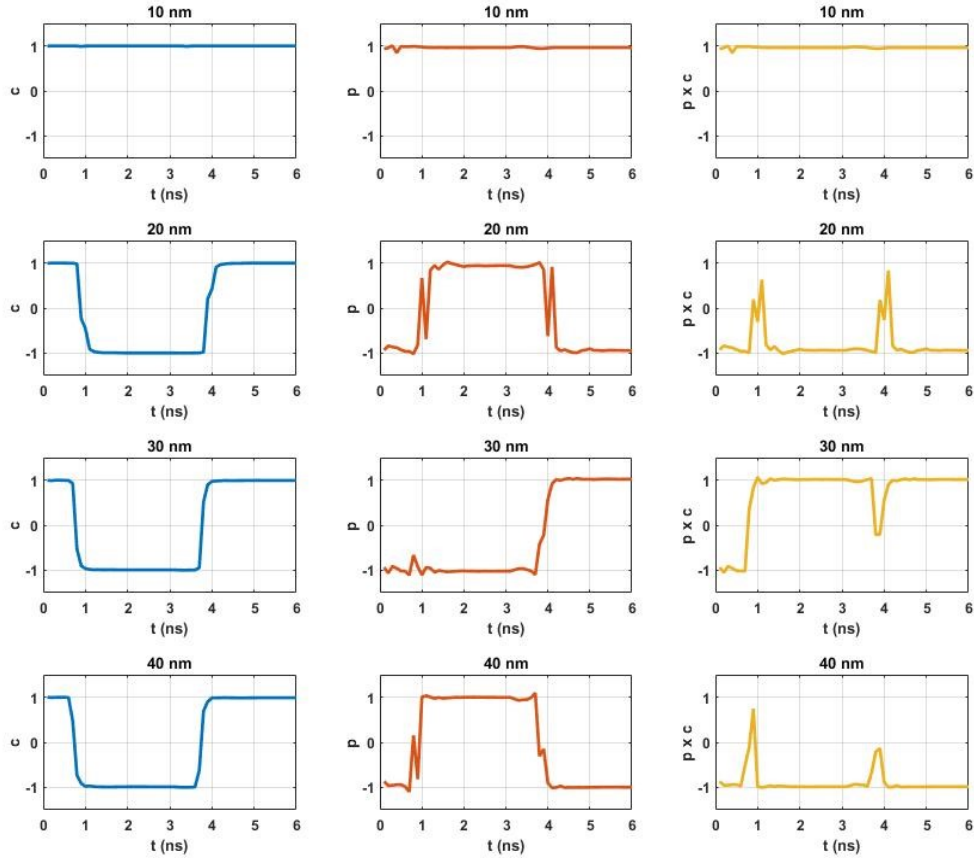
**Figure S4**. The chirality (c, left column of plots), polarity (p, middle column of plots), and sgn(p)×sgn(c) result (right column of results) for 100 nm permalloy nanodiscs of 10 nm, 20 nm, 30 nm, and 40 nm thickness. Note that the 30 nm thick disc signals no coupling of chirality and polarity as the sgn(p)×sgn(c) product changes sign after reversal, meaning c and p behave independent of each other. The peaks in 20 nm and 40 nm thick discs appear due to the transient disorder during switching. The 10 nm disc displays no peaks as reversal has not occurred for the pulse used to generate the above plots. We give here the values other than -1 or +1 for the product arising from the p×c term to avoid disconnected curves when sgn(p)×sgn(c) changes sign.

A way to check if the 4 vortex states are degenerate, i. e. energetically equivalent from a thermodynamic perspective, is to conduct relaxation simulations under zero field from a given initial state as this would provide a basis for the configurations in the discs to attain specific chiral/polar states. To do so we prepared the 100 nm disc at 10, 20, and 30 nm thicknesses, each in the 4 states, and allowed them to relax as shown in Fig. S5. Note that initially "prepared" configurations, although in a vortex phase, are not necessarily in equilibrium and need to relax. Fig. S5 shows the relaxation of exchange energy and demagnetization energy for the discs with three different thicknesses. In the top row, the initial state was in-plane magnetization with a clockwise chirality and a small area in the center with positive polarity. Then the systems quickly relax in about 1 ns under zero external field as one can deduce from the energy curves in Fig. S5. Independent of the initial "prepared" state, all discs relax to the almost same energy densities, meaning that all four possibilities given above are degenerate. Therefore, from a thermodynamic perspective, for instance, a "CCW and negative polarity" state is energetically equivalent to a

"CCW with positive polarity". The same argument holds for all discs of thicknesses considered in our work. Please note that the configurational state might relax into a different one than the initial but all states for all discs relax to the same energy range after around 1 ns.
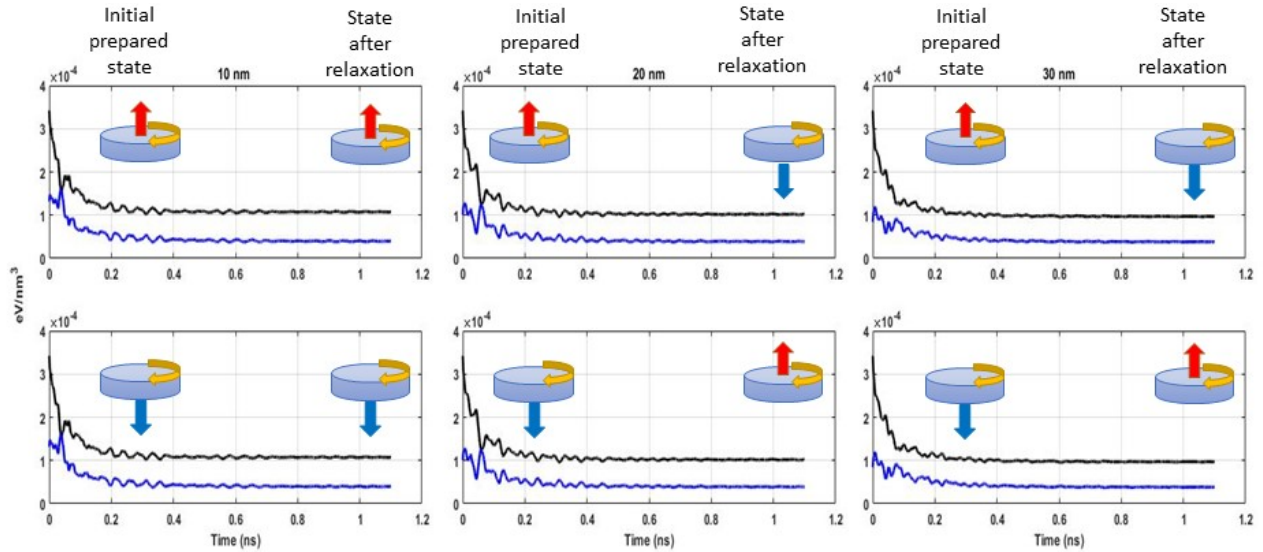


**Figure S5.** Relaxation of vortex states initially set with the same chiralities but different polarities in nanodiscs with different thicknesses. All discs relax to identical energies, implying there is not a tendency for stabilizing in a specific chiral/polar state and that the disc thickness is not a parameter here.

## 7. The effect of disc diameter

Increasing the disc diameter can allow one to reduce the pulse amplitude in order to obtain the same magnetic field distribution with B being around $\approx 0.8$ T near the periphery. This is due to the linear spatial dependence of the field inside the disc as a function of disc radius (See Eq. 8 in the manuscript). Moreover, the reversal process starts from the disc periphery (due to the additional surface energy in these regions and that the field strength is the highest along the periphery). Please check Fig. S6 for the effect of disc diameter on the amount of current to be passed to achieve 0.8 T magnetic field at the disc periphery for 3 different diameters.
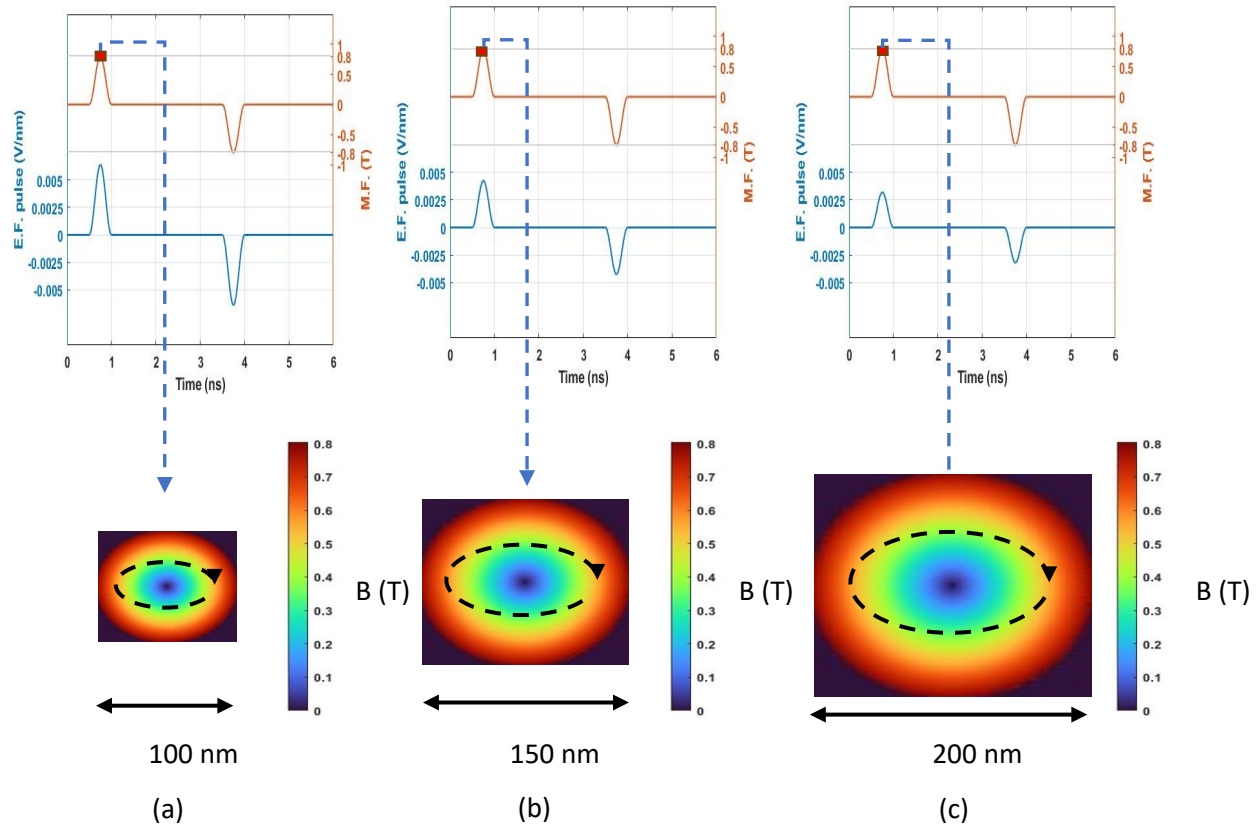
**Figure S6.** Electric pulse and the magnetic field distribution as a function of disc diameter for (a) 100 nm, (b) 150 nm, and (c) 200 nm.

The energy density results obtained from these simulations are shown in Fig. S7. Clearly, by increasing the diameter of the disc and under the same induced magnetic field distribution given in Fig. S6, one can obtain a chirality reversal in 150 nm and 200 nm discs compared to the case of the 100 nm diameter disc where no reversal has occurred. (See Fig. S7 (a,c, and e)). However, in the 10 nm thick discs there is no significant change in energy barriers for the 150 nm and 200 nm ones as shown in (c) and (e). Increasing both the diameter and the thickness reduce fluctuations as well as the demagnetization energy (See Fig. S7 (b, d, and f)), increasing the stability of the magnetic order (this is in fact the well-known size driven effect). The 20 nm thick 100 nm, 150 nm, and 200 nm discs undergo chirality reversal for the same pulse amplitude but one should keep in mind that the greater the disc diameter, the greater the field near the disc periphery, meaning that easier reversal is possible. Therefore, weaker induced magnetic fields could be possible to use to initiate switching (via weaker currents or smaller pulsed field amplitudes, See. Eq. 3 in the manuscript) for larger discs. One can also note that, with increasing diameter of the disc (for 20 nm thickness) the exchange energy peak becomes more dominant than the demagnetizing field: The reason for this is that the magnetic field gets stronger near the disc periphery for large

8

diameters, inducing a more pronounced magnetism on the moments, causing deviation from the parallel ordering of the moments, eventually increasing the exchange contribution (as this energy imposes almost-parallel ordering of moments and during switching this order momentarily disappears, resulting in an increase of this energy term). The demagnetization field is relatively reduced again emanating from the tendency of the majority of the magnetic moments to lie in the plane for larger diameter discs. As mentioned in the manuscript, the demagnetization energy always yields a peak in proportion to the amount of magnetic moment rotation whose normal component transiently intersects the disc plane, generating a discontinuity in the magnetic induction, which in turn causes the appearance of the demagnetization field, hence the demagnetization energy. This energy is relatively smaller in larger diameter discs (such as the 150 nm and 200 nm ones). For smaller diameter discs, due to the size effect, a greater oscillation of the z-component of the magnetic moments is recorded (See Fig. S8 (a)), which in turn causes a greater demagnetization energy peak during switching relative to the exchange peak. Note that the demagnetization energy also oscillates as a result of the z-component of the magnetic moment fluctuation, providing another argument for the size-driven amplification of the demagnetization field. The z-component oscillations of the 150 nm and 200 nm diameter discs are profoundly less significant as much of the "reorientational processes" occur along the x- and y-components of the magnetic moments.
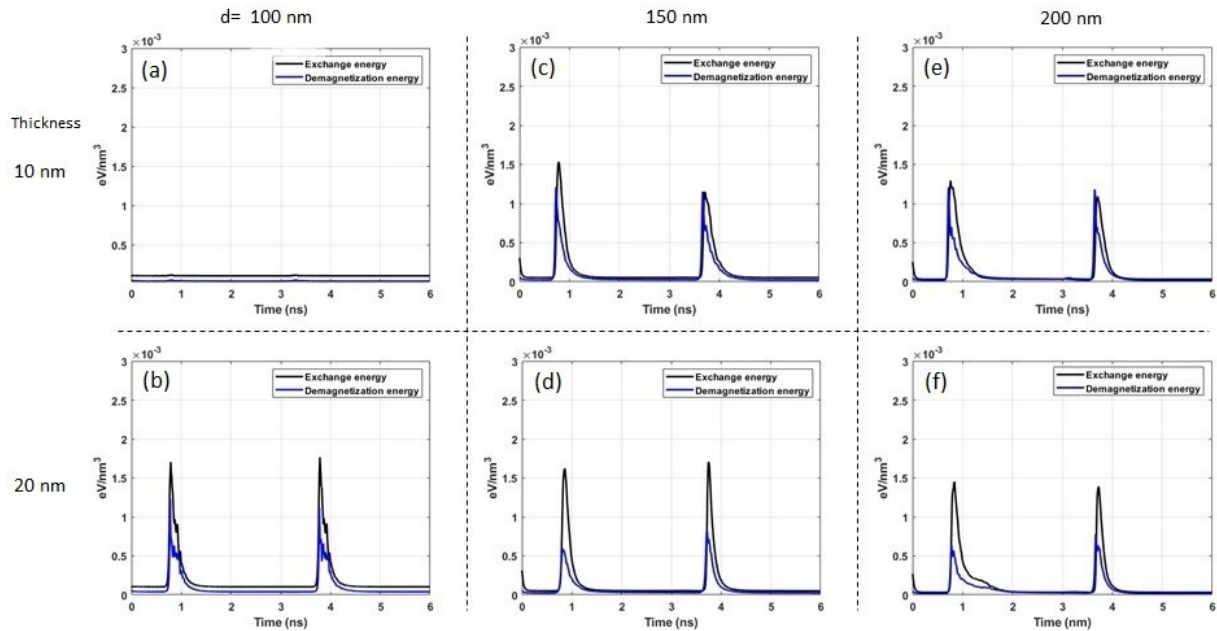


**Figure S7.** Comparison of the exchange and demagnetization energy terms in the left panel: 100 nm in diameter discs (a) 10 nm thick disc, (b) 20 nm thick disc, center panel: 150 nm in diameter discs, (c) 10 nm thick disc, (d) 20 nm thick disc, right panel: 200 nm in diameter discs, (e) 10 nm thick disc, (f) 20 nm thick disc.

As can be seen from Fig. S8, increasing the diameter of the disc allows the magnetic moments a higher freedom to stabilize in the plane of the disc. During the reversal process, the formed vortex core with reversed chirality gyrates around the symmetry center, causing a magnetization wave

with time as shown via the components mx (blue curve) and my (black curve) (Fig. S8 (b) bottom row). The magnetization wave amplitude depends on the gyration orbit. If a vortex core nucleates far away from the symmetry center the magnetization wave is large and it would decay when the vortex core approaches the symmetry center. After the second excitation with the second pulse, we clearly see that the newly formed vortex core with reversed chirality is nucleated near the center, therefore, a small magnetization wave is observed (See Fig. S8 (b, c) bottom). The gyration orbit is shown in Fig. S9 under the first pulse the formed core is far away from the symmetry center and a large gyration orbit is observed which agree with the magnetization wave amplitude (See Fig. S8 (c) bottom). After the second pulse a random configuration is observed (see Fig. S9(b) 3.8 ns). Later, a newly nucleated vortex core emerges at 3.9 ns close to the symmetry center with a small gyration orbit. The magnetization oscillations along the z axis are also decreased with increasing disc diameter as shown in Fig. S8 (b, c) top.
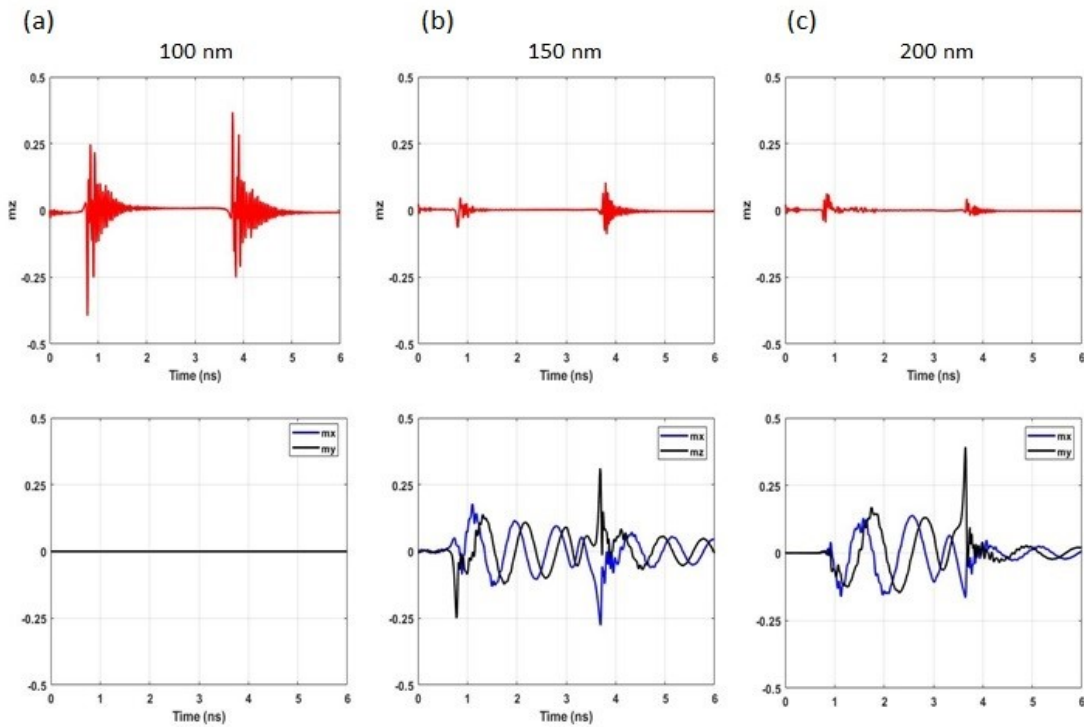


**Figure S8**. The average of the magnetization components mx (blue), my (black), and mz (red) in 20 thick discs in (a) 100 nm in diameter disc, (b) 150 nm in diameter disc, and (c) 200 nm in diameter disc.
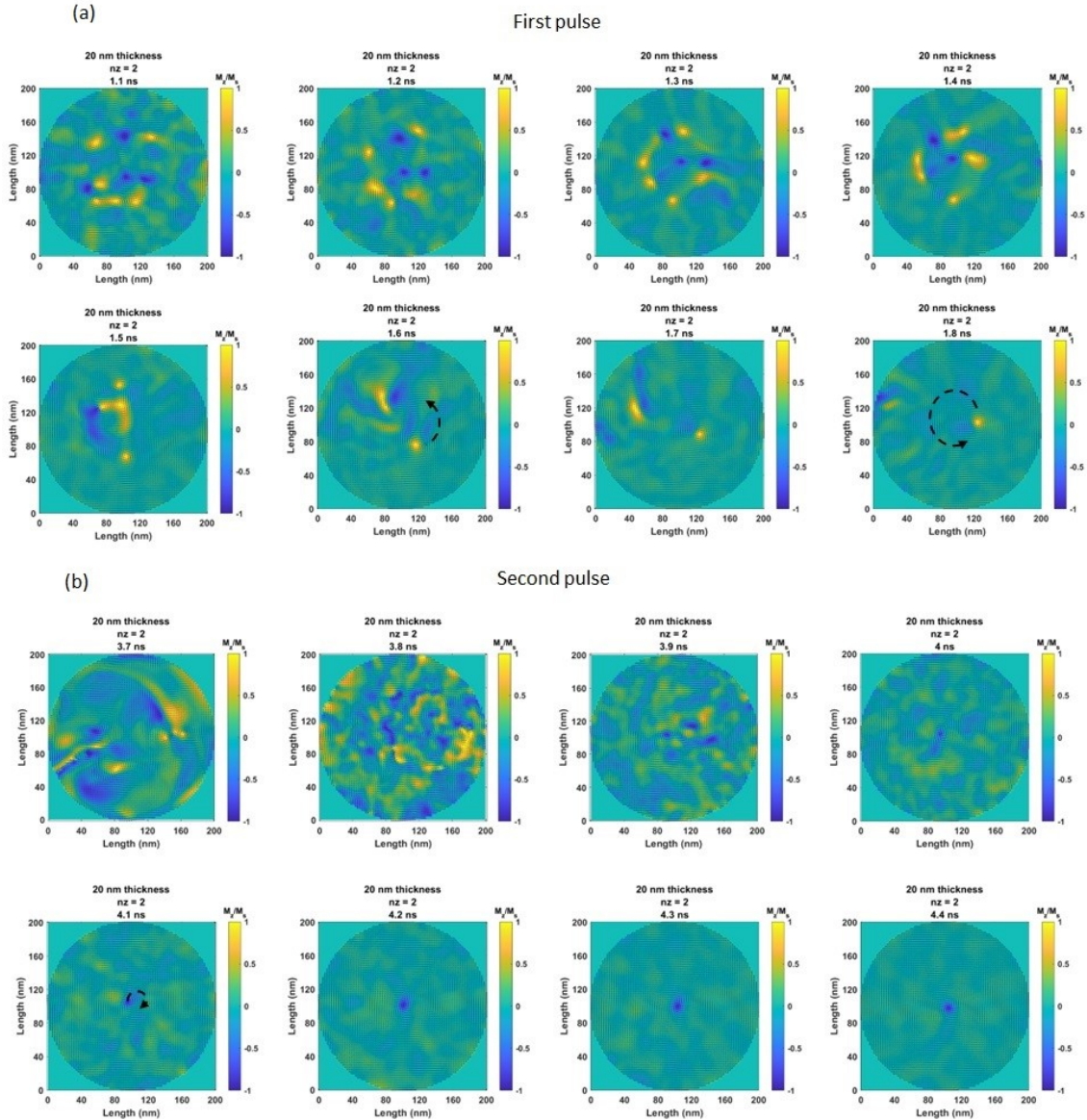
**Figure S9**. The magnetization vectors superimposed on a colormap of the z-component of the magnetization showing the effect of pulses given Fig. S6(c), the black arrows represent the gyration orbit of the newly formed core (a) between the first and the second pulses and (b) after the second pulse.

# References

1.    J. E. Miltat and M. J. Donahue, Handbook of magnetism and advanced magnetic materials **2**, 742-764 (2007).